Oliva Ramírez, Manuel; Schade, Philipp; Zobel, Christoph; Wang, Dong; Schaaf, Peter

Morphological and compositional mapping of supersaturated AuNi alloy nanoparticles fabricated by solid state dewetting

Original published in:	Applied surface science advances. - Amsterdam : Elsevier. - 4 (2021), art. 100082, 6 pp.
Original published:	2021-03-15
ISSN:	2666-5239
DOI:	10.1016/j.apsadv.2021.100082
[*Visited:*	2022-02-23]

Applied Surface Science Advances 4 (2021) 100082

Contents lists available at ScienceDirect

Applied Surface Science Advances

journal homepage: www.elsevier.com/locate/apsadv

Morphological and compositional mapping of supersaturated AuNi alloy nanoparticles fabricated by solid state dewetting

Manuel Oliva-Ramirez*, Philipp Schade[1], Christoph Zobel[1], Dong Wang, Peter Schaaf

TU Ilmenau, Chair Materials for Electrical Engineering and Electronics, Institute of Materials Science and Engineering and Institute of Micro- and Nanotechnologies MacroNano®, Gustav-Kirchhoff-Strasse 5, 98693 Ilmenau, Germany

ARTICLE INFO

Keywords:
Solid state dewetting
Supersaturated alloys
Tailored design
Nanometallurgy
AuNi alloys
Supersaturated alloy decomposition

ABSTRACT

The solid state dewetting (SSD) of metallic bilayers is a straightforward method for the fabrication of alloy nanoparticles. In particular, alloys that present a gap of miscibility offer a rich phenomenology regarding not only the particle formation but also the composition of their phases. In the present work, AuNi precursor bilayers have been annealed at different temperatures and times to produce AuNi alloy nanoparticles. The evolution of the shape, size, and interparticle distance as well as the composition of the different phases formed in the nanoparticles, allow to unravel the role of the annealing temperatures and times for the fabrication of AuNi supersaturated alloys. Furthermore, the results offer a morphological and compositional map for the fabrication of AuNi alloys nanoparticles of different shapes, sizes, and compositions. Therefore, this map is a useful tool for the tailored design of supersaturated or decomposed nanoparticles by SSD.

1. Introduction

The solid-state dewetting (SSD) of thin films received much attention in the past for causing the failure in micro- and nano-electronic components. However, in the recent years the targeted dewetting of thin films became an interesting field of research for the fabrication of arrays of nanoparticles [1–5]. One of the assets of SSD is that it provides a fast and straightforward way to produce nanoparticles from either single component or bilayer metallic thin films, which means a cost-effective alternative to chemical methods [6–10].

While the SSD of single component films has been profusely studied in the past, SSD of metallic bilayers or binary alloys presents a more complex scenario and offers a richer phenomenology because the composition of the forming phases might also play a role in the particle formation. The understanding of this role supposes an extra tool in SSD for the tailored design of nanoparticles or nanoalloys presenting a particular shape, size, or distribution as well as composition. This way, the SSD of Co-Pd alloys presented an intermediated morphology and dewetting rate that those of the elemental materials [11]. More interesting resulted the alloying with Pt in Au-Pt systems, which kinetically hindered the diffusivity of the alloy and delayed the voids formation and growth [12,13]. Similar results were obtained in Au–Fe bilayers, where the Fe underlayer provided a higher thermal stability against SSD. Moreover, in the formed nanoparticles Fe-rich phase precipitates were controlled by the annealing conditions [14,15]. As an example of an immiscible system, Co–Au lead to the formation of independent Au-rich and Co-rich nanoparticles [11].

The SSD of AuNi bilayers to form alloys is a particularly interesting case because Au and Ni present a miscibility gap [16]. Tuning the thermal process by annealing above the miscibility gap and rapidly cooling down to room temperature to freeze the compound is possible to obtain supersaturated AuNi alloys in different shapes such as layers with hollows or independent nanoparticles [17–20]. Previous works focused on the influence of different annealing temperatures on the morphology and alloying state of the formed nanoparticles for a fixed time however, the influence of the annealing time in the evolution of the morphology and alloying state remained unexplored. In this work, we study the SSD of AuNi bilayers at different temperatures above the miscibility gap and for different annealing times. By the analysis of the evolution of shape and size of the nanoparticles together with the composition of the formed phase, we unravel the roles of annealing temperatures and times, being the later a new complementary parameter to use as tool. Furthermore, we provide a morphological and compositional map of AuNi alloy nanoparticles that offers a useful kit for the tailored design of nanoparticles.

2. Materials and methods

2.1. Deposition of the precursor AuNi bilayer

Metallic bilayers of Au and Ni were deposited by electron beam in an Ardenne CS 400 ES PVD-cluster system. The bilayers were fabricated

* Corresponding author.
E-mail address: manuel.oliva-ramirez@tu-ilmenau.de (M. Oliva-Ramirez).
[1] These authors have contributed equally.

https://doi.org/10.1016/j.apsadv.2021.100082
Received 2 October 2020; Received in revised form 1 March 2021; Accepted 3 March 2021

by the deposition of 10 nm of Ni and the subsequent deposition of another 10 nm of Au on top. The films were grown at a working pressure of $1 \cdot 10^{-6}$ mbar and their thicknesses were controlled by a quartz balance. A p-type silicon wafer with (100)-orientation (conductivity < 0.005 Ω•cm) was used as substrate. To prevent any interaction between Si and the metallic material, an SiO_2 layer of 100 nm was thermally grown prior deposition at 1050 °C for 55 min in a furnace with dry oxygen atmosphere.

2.2. Thermal treatments

Thermal annealing processes of the AuNi bilayers were carried out by a flash light in an RTP Jipelec Jetfirst 100. The treatments consist of a pre-heating of the chamber at 300 °C for 1 min and after that, a rapid heating (within 10 s) to the desired temperature (875, 900, 925 and 950 °C) and annealing at that temperature for a given annealing time (1, 5, 10 min), followed by rapid cooling (see Fig. A13 for details). A reducing atmosphere of H_2 (50 sccm) and Ar (1500 sccm) was maintained inside the chamber during the process and until it cooled down to about room temperature to avoid the oxidation of the Ni phase. We used a fresh precursor AuNi bilayer for each treatment, a total of 12 samples. In the text, we will refer to the systems as AuNi-followed by the temperature and the duration of the annealing. This way, the system annealed at 875 °C for 1 min will be labeled as "AuNi-875C-1min". We will use the label AuNi-temperature to refer to all the systems annealed at that temperature, i.e., the three systems annealed at 875 °C will be called "AuNi-875C".

2.3. Characterization

Scanning electron microscopy (SEM) pictures of the treated samples were recorded in a Hitachi-S4800. Both secondary electrons (SE) and backscattered electron (BSE) detectors were used to characterize the morphology and to find out information about the composition, respectively. Because elements with higher atomic number backscatter more electrons, in the BSE mode, the Au phase appears brighter than the Ni phase, meanwhile their alloys present an intermediated contrast.

To determine the phase composition and crystallinity of the treated samples, X-ray diffraction (XRD) analyses were performed at Bragg-Brentano configuration in a Siemens D-5000 diffractometer employing Cu-Kα radiation. 2θ angles from 36° to 56° were recorded because both Au and Ni present their most characteristic diffraction reflexes in this range, i.e. those that correspond to the (111) and (200) orientations. The powder diffraction files PDF65-2870 and PDF04-0850 were used to identify in the diffractograms the orientations of the reflexes of Au and Ni, respectively [21].

ImageJ software was used to determine from SEM pictures the interparticle distance, the particle size, and the circularity of the formed nanoparticles after the annealing treatments [22]. The interparticle distance was estimated from the first maxima of the normalize correlation functions. The particle size was calculated by measuring the area of the nanoparticles and considering them circular, so the size was $size = 2\sqrt{area/\pi}$. The circularity by its part, was determined by applying the equation $circularity = 4\pi(area/perimeter^2)$.

3. Results

3.1. Morphology of annealed AuNi bilayers at different temperatures and annealing times

Fig. 1 presents an overview of the AuNi precursor bilayers after thermal treatments at different temperatures and annealing times. At a first glance, it shows that the annealing at lower temperatures (AuNi-875C, AuNi-900C) lead to the formation of larger and more elongated particles than those at higher temperatures (AuNi-925C, AuNi-950C), which

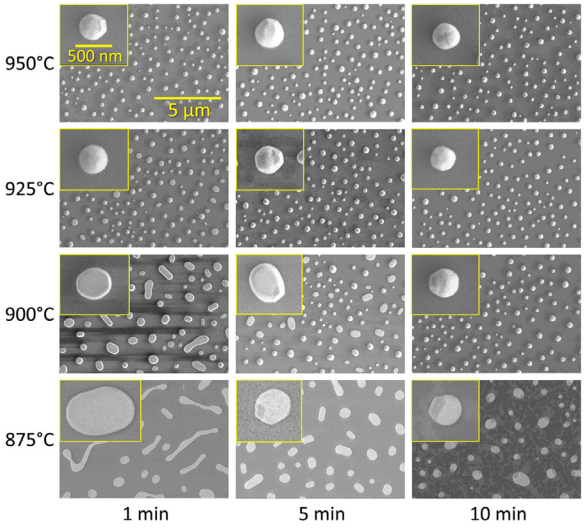

Fig. 1. SEM pictures of the formed particles after annealing the AuNi precursor bilayers for different annealing temperatures and times. The insets show a selected representative particle of each system.

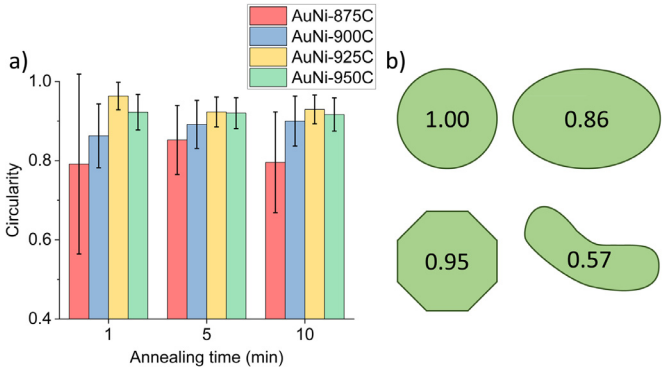

Fig. 2. a) Mean circularity of the nanoparticles formed in the systems as a function of the annealing time for the different systems. The error bars represent the standard deviation. The mean circularities were determined from the histograms of the circularities, which can be found in the panels b) of figures A1 to A12 of the appendix information. b) Circular, oval, elongated and polyhedral shapes and their corresponding circularities.

are smaller and more spherical. These elongated and oval nanoparticles are particularly noticeable in the AuNi-875C-1min and they do not longer form in the systems AuNi-925C and AuNi-950C, and in AuNi-900C-10min.

To quantify these observations about the shape, size and spatial distribution of the nanoparticles, SEM pictures of larger areas (2800 µm^2) than those presented in Fig. 1 (110 µm^2) were analyzed and can be found in the panels a) of figures from A1 to A12 of the Appendix. Fig. 2a) presents their mean circularity C in the different systems, which is defined by $C = 4\pi \cdot A/P$, where area A and perimeter P refer to those of the nanoparticles. This parameter is a shape descriptor that compares the actual area of the nanoparticles to that of a virtual circle of radius determined by the perimeter ($r = P/2\pi$). That way, as shows Fig. 2b), a perfect circular particle presents a circularity of 1 by definition and elongated, oval or faceted particles are always below that value. Fig. 2a) exhibits that the nanoparticles are more elongated at lower temperatures and that they became more circular with longer annealing times and increasing temperatures.

This evolution becomes more noticeable when considering the standard deviations from the mean values, which are included as error bars in Fig. 2a). The decreasing values of the standard deviations indicate

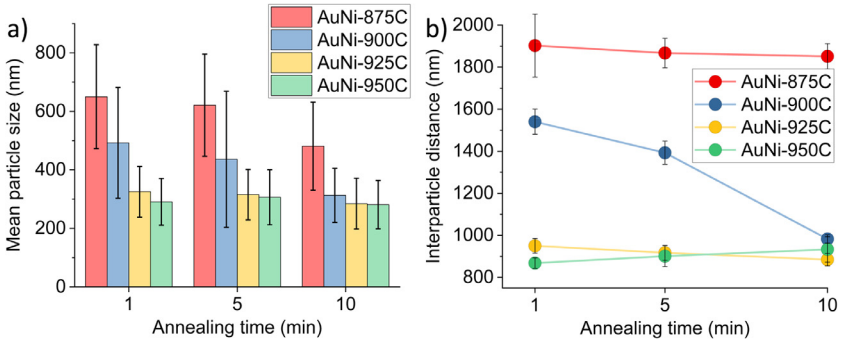

Fig. 3. Mean particle size a), and interparticle distance (connecting lines are only to guide the eyes) b) of the dewetted particles as a function of the annealing time for the different systems. The mean particle sizes were calculated from the histograms of the particles sizes presented in the panels c) of figures A1 to A12 of the appendix. The interparticle distances were determined from the first maxima of the normalized correlation function of the systems and are included in the panels d) of figures A1 to A12 of the Appendix.

the increasing homogeneity of the shape of the nanoparticles with the increasing annealing times and temperatures.

The mean particle size of the nanoparticles of the systems in Fig. 3a) reveals two clear tendencies. On the one hand, the particle size decreases with increasing temperatures for the same annealing times, and on the other at a given temperature the particle size decreases with longer annealing times. This decreasing size of the nanoparticles seems to present a limit about 300 nm regardless of the annealing time.

In Fig. 3b) the averaged interparticle distance depends on the temperature similarly to the mean particle size, i.e., higher temperatures lead to shorter interdistances. As regards to the annealing time, the interparticle distance is not considerable affected except in the systems AuNi-900C, where it clearly decreases with increasing annealing times. The systems AuNi-950C show a deviation of the main trend and their interparticle distance slightly increases with longer annealing times. The evolution of the different systems points to a minimum interdistance of about 900 nm.

A closer view of the different systems in the insets of Fig. 1 allows to identify two different phases in the nanoparticles thanks to the material contrast. Regarding to their shape, for a given annealing time the particles evolve from large flat particles to truncated polyhedrons with increasing annealing temperatures. In the cases of given temperatures, longer annealing times lead to more faceted nanoparticles. Only the system AuNi-950C-10min does not follow these trends and presents spherical shapes with mixed darker areas.

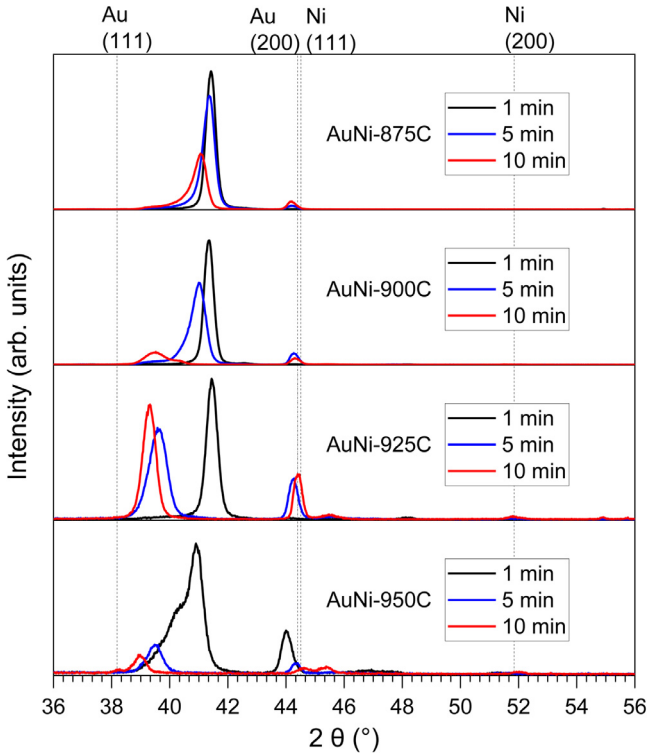

Fig. 4. XRD pattern of the dewetted systems.

3.2. *Phase formation in dewetted AuNi bilayers as a function of temperature and annealing time*

To determine the phases formed after SSD in the systems, Fig. 4 shows their XRD diffractograms.

All the systems present a main reflex between Au (111) and Ni (111) that indicates the formation of supersaturated AuNi alloy nanoparticles and that is identified as their (111) orientation [23]. Most of the systems also show a small reflex shifted rightward from Ni (111) pointing the formation of Ni-rich phases.

In the systems AuNi-875C-1min, AuNi-900C-1min, and AuNi-925C-1min, a single reflex appears about 41.5° indicating the formation of a single phase of supersaturated AuNi alloy. Longer annealing times at those temperatures lead to a shift leftwards of the AuNi supersaturated reflexes, and to raise a reflex about 44.2°, which indicates a rather pure Ni-rich phase. It is worth noting that with increasing temperatures the reflexes belonging to the supersaturated phases shift leftward, meanwhile the intensity of the reflexes of the Ni-rich phase just increases.

The systems AuNi-950C presented a different trend. AuNi-950C-1min shows a main reflex corresponding to a supersaturated AuNi alloy with a shoulder at its left side, and a Ni-rich phase. The shoulder is the result of a convolution of a third phase consisting in a Au-rich AuNi phase. The diffractogram of AuNi-950C-5min is similar to those recorded for other temperatures, but AuNi-950C-10min presents small reflexes about 45° that we attribute to the orientation (200) of the Au-rich phase, and to the (200) orientation of the remaining AuNi supersaturated alloy.

The composition of the phases forming the nanoparticles can be determined from the position of the reflexes in the diffractograms, which provides their lattice spacing. *Crawley* and *Fabian* demonstrated that Vegard's law cannot be applied to AuNi supersaturated alloys because the actual values differ from the theoretical predictions. Therefore, they investigated those deviations and determined the actual composition as a function of the lattice spacing [24]. Following that correction, Table 1 presents the composition of the AuNi supersaturated phase of the nanoparticles determined from the position of their reflexes. As the precursor bilayers consisted of a Ni and a Au layers of 10 nm of thickness, the expected composition should be 39 at% Au and 61 at% Ni. Those values are in good agreement with the systems AuNi-875C-1min, AuNi-900C-1min, and AuNi-925C-1min, although they present slight deviations that can be caused by marginal stresses due to quenching or evaporation effects during annealing [25]. For the other systems, as commented above, the supersaturated alloy phase shift from the expected composition. To visualize this evolution of the phases, Fig. 5 depicts the compositions calculated in Table 1. It shows that both longer annealing

Table 1
Lattice spacing and derived composition of the different systems calculated from the tabulation of Crawley and Fabian [24].

System	(111) AuNi reflex position 2θ [°]	Lattice spacing a_0 [nm]	x Au, atomic fraction [%]	x Ni, atomic fraction [%]
AuNi-875C-1min	41.42	0.377	37	63
AuNi-875C-5min	41.36	0.378	39	61
AuNi-875C-10min	41.06	0.380	42	58
AuNi-900C-1min	41.36	0.378	39	61
AuNi-900C-5min	41.00	0.381	44	56
AuNi-900C-10min	39.52	0.395	71	29
AuNi-925C-1min	41.44	0.377	37	63
AuNi-925C-5min	39.58	0.394	69	31
AuNi-925C-10min	39.32	0.397	75	25
AuNi-950C-1min	40.90	0.382	46	54
AuNi-950C-5min	39.48	0.395	71	29
AuNi-950C-10min	38.98	0.400	82	18

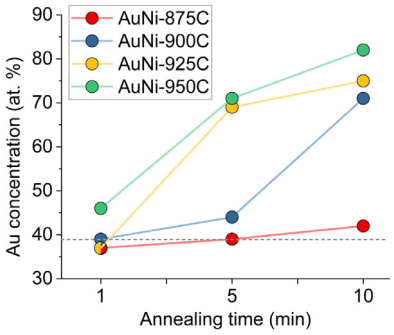

Fig. 5. Composition of the (111) supersaturated AuNi alloy phases. The lines connecting the dots are just to guide the eye. The dashed line represents the deposited concentration.

times and higher temperatures lead to an increase of the Au concentration in the (111) supersaturated alloy phase and therefore, a decrease of the Ni concentration. This Au enrichment and Ni decay in the supersaturated phases is complemented by the Ni-rich phases, which gathers the excess Ni.

In Fig. 1, the nanoparticles of the systems that exhibit a single phase in the XRD analysis, i.e. AuNi-875C-1min, AuNi-900C-1min, and AuNi-925C-1min, present a homogeneous contrast over their surface. In the nanoparticles of the rest of the systems, a darker and more faceted second phase appears that we identify with the Ni-rich phase due to the smaller atomic number of Ni with respect to Au. At a given temperature, these separated phases become larger with longer annealing times, which is particularly noticeable in the systems AuNi-875C. Besides, the particular morphology of the system AuNi-950C-10min coincides with its singular diffractogram commented above.

4. Discussion

4.1. SSD of AuNi precursor bilayers and particle formation

The morphologies observed in Fig. 1 correspond with the latest stages of SSD, at which the rims of the holes already broke up into elongated nanoparticles (also called fingers) that might undergo Rayleigh's instabilities splitting up into smaller particles [26,27]. The particles that are too small to split will evolve towards circular shapes first to minimize the surface energy, and eventually towards the equilibrium crystal shape (ECS) forming polyhedrons [28,29]. The system AuNi-875C-1min clearly exhibits this fingering phenomenon and it is possible to observe an incipient narrowing in some of the elongated particles that point where the particles would have split in the case of longer annealing times. The evolution time scale for Rayleigh's instabilities ($t_{Rayleigh}$) under surface-diffusion-dominated transport obeys the following dependence [26,30]:

$$t_{Rayleigh} \propto \frac{R_{cyl}^4}{D_s} \quad (1)$$

where D_s is the surface diffusivity and R_{cyl} is the radius of the elongated particle approximated to a cylinder. According to this equation, higher temperatures will increase the surface diffusivity reducing the time scale needed for Rayleigh's instabilities to occur. Therefore, at higher temperatures or longer annealing times these elongated particles would split into smaller ones. This effect together with the minimization of the surface energy lead to the absence of elongated particles in the systems AuNi-925C and AuNi-950C, and in the system AuNi-900C-10min.

The analysis of the circularity and the insets of Fig. 1 shows the formation of more circular particles with increasing annealing times for the systems AuNi-875C and AuNi-900C. The systems AuNi-925C and AuNi-950C present a circularity about 0.9 independently of the annealing time. This points a different evolution related with their dewetted state. Meanwhile in AuNi-875C and AuNi-900C the particles split into smaller ones and become more spherical to minimize the surface energy, in AuNi-925C and AuNi-950C they evolved towards the ECS decreasing slightly their circularity.

The mean particle size together with the interparticle distance bring more light about the evolution of the nanoparticles. In the systems AuNi-875C the mean particle size decreases and the interparticle distance remain practically constant, which suggests the splitting of elongated nanoparticles and their subsequent retraction. The particle size of the systems AuNi-900C also decreases for longer annealing times however, the interparticle distance decreases too considerably. The latter points the splitting of oval particles whose formed particles remain closer. For the systems AuNi-925C and AuNi-950C there are no significant changes pointing that the SSD is already accomplished after 1 min.

Furthermore, the evolution of the systems exposes both lower limits, the mean particle size (~300 nm) and the interparticle distance (~900 nm). The wavelength of the Rayleigh's instabilities that determines the size of the splitting nanoparticles depends on the cylinder radius rather than on the temperature, which affects the time required for the splitting to occur [27]. This way, these limits are determined by the thickness of the deposited precursor bilayers and cannot be further reduced even with longer annealing times or higher annealing temperatures.

4.2. Supersaturated AuNi alloys: formation and decomposition

The systems AuNi-875C-1min, AuNi-900C-1min, and AuNi-925C-1min, present single phase supersaturated AuNi alloy as a result of the annealing over the miscibility gap and a subsequent fast cooling that

freeze the alloy. The highly texturing is the result of the minimization of the surface energy. In the case of a FCC structure as is the present case, the texture (111) exhibits the lowest surface energy [25]. The formation of a single phase in those systems indicates that 1 min of annealing time at those temperatures is enough to fully mix both phases even at solid state [31]. Therefore, the enrichment of Au of the supersaturated AuNi alloy phases and the Ni-rich phases that appears in the other systems, must be the result of the decomposition of the AuNi alloys. This decomposition takes place during the cooling step, which is not fast enough in those cases to freeze the supersaturated alloys. The cooling rates for the systems AuNi-900C presented in figure A13 of the appendix, shows that for longer annealing times the cooling rate of the chamber is much lower. This happens because our annealing set up lack of active cooling and therefore, longer annealing times leads to higher residual heats, which in turn, slow down the cooling assisting the decomposition of the supersaturated alloys. The same effect takes place in the systems AuNi-950C due to their higher temperature. At the studied composition (61 at% Ni), the miscibility gap starts below 786 °C and the end of the atoms mobility should be around 220 °C according to Tamman's rule ($0.4 \times T_s$, with the melting temperature of the AuNi alloy T_s=1227 K) [32]. Therefore, longer annealing times and higher temperatures lead to more decomposition of the AuNi alloys.

Once unraveled the role of the residual heat, it can be correlated with the decomposition state of the systems. In the systems AuNi-875C and AuNi-900C the ongoing decomposition affects the crystallinity of the samples with a considerably decrease of the (111) orientation as the Ni-rich phase appears. The systems AuNi-925C by their part, present better defined reflexes and their increase for the system AuNi-925C-10min indicates that the phase separation already took place and that the nanoparticles evolve towards the ECS increasing considerably their crystallinity. This can be clearly observed in Fig. 1. At the higher temperature studied here, the decomposition already starts in the AuNi-950C-1min. The AuNi-950C-10min also exhibits a weak (200) Au-rich phase associated to a decrease of the strain energy in the supersaturated alloy [33], which points that the decomposition mechanism was different than in the other cases. An overall conclusion from these behaviors is that the decompositions begin by the segregation of a rather pure Ni-rich phase from the alloy, which is in good agreement with the founding of Herz et al. [17].

5. Conclusions

Supersaturated AuNi alloy nanoparticles of different shape, size and composition were successfully produced by the SSD of AuNi bilayers. Most of these nanoparticles were highly textured and exhibited supersaturated phases whose composition depends on the thermal treatments. Thus, the role of the cooling rate has been proved to be crucial for the final composition. Only the systems AuNi-875C-1min, AuNi-900C-1min, and AuNi-925C-1min, presented single phase supersaturated AuNi alloy. In the other systems, the supersaturated alloy phase decomposed due to the residual heat inside the annealing chamber, which triggers the phase separation below the miscibility gap. Moreover, it was found that the decomposition of the supersaturated AuNi alloys starts with the segregation of a Ni-rich phase.

Regarding the morphology of the systems, the particle size decreased with increasing temperatures for the same annealing times, and at a given temperature the particle size decreases with longer annealing times. Also, the shape of the particles evolved from elongated at lower temperatures, to circular with longer annealing times and increasing temperatures. Furthermore, we found the lower achievable limits of mean particle size (~300 nm) and interparticle distance (~900 nm) from a bilayer of 10 nm of Au and 10 nm of Ni by SSD.

These results exhibit the tendencies of the SSD of precursor bilayers and provide a morphological and compositional map of AuNi alloy nanoparticles that offers a useful tool for the tailored design of nanoparticles.

Acknowledgments

The work is supported by the Deutsche Forschungsgemeinschaft (DFG, grant Scha 632/20, FunPartY). This work is also supported by the free state of Thuringia under grants 2015 FGI 0025 305 (FastμXRD) and B715-10009 (BioMacroNano2020), all co-financed by the European Union within the framework of the European Regional Development Fund (ERDF). We are grateful to Joachim Döll from the TU Ilmenau ZMN, who helped in the preparation of the samples.

Supplementary materials

Supplementary material associated with this article can be found, in the online version, at doi:10.1016/j.apsadv.2021.100082.

References

[1] F. Leroy, Ł. Borowik, F. Cheynis, Y. Almadori, S. Curiotto, M. Trautmann, J.C. Barbé, P. Müller, How to control solid state dewetting: a short review, Surf. Sci. Rep. 71 (2016) 391–409, doi:10.1016/j.surfrep.2016.03.002.
[2] D. Wang, R. Ji, P. Schaaf, Formation of precise 2D Au particle arrays via thermally induced dewetting on pre-patterned substrates, Beilstein J. Nanotechnol. 2 (2011) 318–326, doi:10.3762/bjnano.2.37.
[3] B.T. Schaefer, J. Cheung, J.F. Ihlefeld, J.L. Jones, V. Nagarajan, Stability and dewetting kinetics of thin gold films on Ti, TiOx and ZnO adhesion layers, Acta Mater. 61 (2013) 7841–7848, doi:10.1016/j.actamat.2013.09.022.
[4] F. Ruffino, M.G. Grimaldi, Template-confined dewetting of Au and Ag nanoscale films on mica substrate, Appl. Surf. Sci. 270 (2013) 697–706, doi:10.1016/j.apsusc.2013.01.130.
[5] L.-X. Lu, Y.-M. Wang, B.M. Srinivasan, M. Asbahi, J.K.W. Yang, Y.-W. Zhang, Nanostructure formation by controlled dewetting on patterned substrates: a combined theoretical, modeling and experimental study, Sci. Rep. 6 (2016) 32398, doi:10.1038/srep32398.
[6] S. Zhou, H. Yin, V. Schwartz, Z. Wu, D. Mullins, B. Eichhorn, S.H. Overbury, S. Dai, situ phase separation of NiAu alloy nanoparticles for preparing highly active Au/Nio CO oxidation catalysts, ChemPhysChem 9 (2008) 2475–2479, doi:10.1002/cphc.200800587.
[7] Y.S. Wu, S. Bagchi, S. Garg, N. Singh, T. Tsai, SCIDIVE: a stateful and cross protocol intrusion detection architecture for voice-over-IP environments, in: Proceedings of the International Conference on Dependable Systems and Networks, 2004, pp. 433–442, doi:10.1021/nl035162i.
[8] V. Schmidt, J.V. Wittemann, U. Gösele, Growth, thermodynamics, and electrical properties of silicon nanowires, Chem. Rev. 110 (2010) 361–388, doi:10.1021/cr900141g.
[9] R. Ferrando, J. Jellinek, R.L. Johnston, Nanoalloys: from theory to applications of alloy clusters and nanoparticles, Chem. Rev. 108 (2008) 845–910, doi:10.1021/cr040090g.
[10] C.V. Thompson, Solid-state dewetting of thin films, Annu. Rev. Mater. Res. 42 (2012) 399–434, doi:10.1146/annurev-matsci-070511-155048.
[11] R. Esterina, X.M. Liu, A.O. Adeyeye, C.A. Ross, W.K. Choi, Solid-state dewetting of magnetic binary multilayer thin films, J. Appl. Phys. 118 (2015), doi:10.1063/1.4932565.
[12] C.Manuela Müller, R. Spolenak, Dewetting of Au and AuPt alloy films: a dewetting zone model, J. Appl. Phys. 113 (2013), doi:10.1063/1.4794028.
[13] A. Jedele, Die diffusion im festen zustand bei den metallpaaren gold-nickel, gold-palladium und gold-platin, Z. Elektrochem. Angew. Phys. Chem. 39 (1933) 691–695, doi:10.1002/bbpc.19330390810.
[14] D. Amram, L. Klinger, E. Rabkin, Anisotropic hole growth during solid-state dewetting of single-crystal Au-Fe thin films, Acta Mater. 60 (2012) 3047–3056, doi:10.1016/j.actamat.2012.02.009.
[15] D. Amram, L. Klinger, E. Rabkin, Phase transformations in Au(Fe) nano-and microparticles obtained by solid state dewetting of thin Au-Fe bilayer films, Acta Mater. 61 (2013) 5130–5143, doi:10.1016/j.actamat.2013.04.062.
[16] C. Wolverton, A. Zunger, Ni-Au: a testing ground for theories of phase stability, Comput. Mater. Sci. 8 (1997) 107–121, doi:10.1016/s0927-0256(97)00023-2.
[17] A. Herz, M. Friák, D. Rossberg, M. Hentschel, F. Theska, D. Wang, D. Holec, M. Šob, O. Schneeweiss, P. Schaaf, Facet-controlled phase separation in supersaturated Au-Ni nanoparticles upon shape equilibration, Appl. Phys. Lett. 107 (2015), doi:10.1063/1.4928627.
[18] A. Herz, F. Theska, D. Rossberg, T. Kups, D. Wang, P. Schaaf, Solid-state dewetting of Au–Ni bi-layer films mediated through individual layer thickness and stacking sequence, Appl. Surf. Sci. 444 (2018) 505–510, doi:10.1016/j.apsusc.2018.03.096.
[19] D. Wang, P. Schaaf, Ni-Au bi-metallic nanoparticles formed via dewetting, Mater. Lett. 70 (2012) 30–33, doi:10.1016/j.matlet.2011.11.102.
[20] A. Herz, D. Wang, R. Müller, P. Schaaf, Formation of supersaturated Au-Ni nanoparticles via dewetting of an Au/Ni bilayer, Mater. Lett. 102–103 (2013) 22–25, doi:10.1016/j.matlet.2013.03.096.
[21] E.R. Jette, F. Foote, Precision determination of lattice constants, J. Chem. Phys. 3 (1935) 605–616, doi:10.1063/1.1749562.
[22] C.A. Schneider, W.S. Rasband, K.W. Eliceiri, NIH image to ImageJ: 25 years of image analysis, Nat. Methods 9 (2012) 671–675, doi:10.1038/nmeth.2089.

[23] A. Herz, D. Wang, R. Müller, P. Schaaf, Formation of supersaturated Au–Ni nanoparticles via dewetting of an Au/Ni bilayer, Mater. Lett. 102–103 (2013) 22–25, doi:10.1016/j.matlet.2013.03.096.
[24] A.F. Crawley, D.J. Fabian, A redetermination of the lattice spacings and densities of gold-nickel solutions, J. Inst. Metals 94 (1965) 39–40.
[25] A. Herz, On the Solid-State Dewetting of Au-Ni and Au-W Bilayer Polycrystalline Thin Films and the Formation of Alloy Micro- and Nanoparticles, Technische Universität Ilmenau, 2016 Dissertation.
[26] C.V. Thompson, Solid-state dewetting of thin films, Annu. Rev. Mater. Res. 42 (2012) 399–434, doi:10.1146/annurev-matsci-070511-155048.
[27] D.T. Danielson, D.K. Sparacin, J. Michel, L.C. Kimerling, Surface-energy-driven dewetting theory of silicon-on-insulator agglomeration, J. Appl. Phys. 100 (2006), doi:10.1063/1.2357345.
[28] G. Wulff, XXV. Zur frage der geschwindigkeit des wachsthums und der auflösung der krystallflächen, Z. Krist. – Crystall. Mater. 34 (1901), doi:10.1524/zkri.1901.34.1.449.
[29] W. Jiang, Y. Wang, Q. Zhao, D.J. Srolovitz, W. Bao, Solid-state dewetting and island morphologies in strongly anisotropic materials, Scr. Mater. 115 (2016) 123–127, doi:10.1016/j.scriptamat.2016.01.018.
[30] F.A. Nichols, W.W. Mullins, Morphological changes of a surface of revolution due to capillarity-induced surface diffusion, J. Appl. Phys. 36 (1965) 1826–1835, doi:10.1063/1.1714360.
[31] A. Herz, D. Wang, Th. Kups, P. Schaaf, Solid-state dewetting of Au/Ni bilayers: the effect of alloying on morphology evolution, J. Appl. Phys. 116 (2014) 044307, doi:10.1063/1.4891448.
[32] B. Predel, Au-Ni (gold-nickel): supplement, in: B. Predel (Ed.), Ac-Ag ... Au-Zr, Springer, Berlin, Heidelberg, 2006, pp. 1–3, doi:10.1007/10793176_237.
[33] D. Wang, P. Schaaf, Ni–Au bi-metallic nanoparticles formed via dewetting, Mater. Lett. 70 (2012) 30–33, doi:10.1016/j.matlet.2011.11.102.

Update

Applied Surface Science Advances

Volume 5, Issue , 1 September 2021, Page

DOI: https://doi.org/10.1016/j.apsadv.2021.100108

Applied Surface Science Advances 5 (2021) 100108

Contents lists available at ScienceDirect

Applied Surface Science Advances

journal homepage: www.elsevier.com/locate/apsadv

Erratum regarding missing Declaration of Competing Interest statements in previously published articles

Declaration of Competing Interest statements were not included in the published version of the following articles that appeared in previous issues of Applied Surface Science Advances.

The appropriate Declaration/Competing Interest statements, provided by the Authors, are included below.

1. "Room temperature operated HgCdTe colloidal quantum dot infrared focal plane array using shockwave dispersion technique" [Applied Surface Science Advances, 2020; 1: 100024] https://doi.org/10.1016/j.apsadv.2020.100024.

   Declaration of competing interest: The Authors have no interests to declare.

2. "Fabrication and characterization of extrinsic electrochemically modified graphite reinforcement carbon paste electrode for selective determination of Cu(II) in trace levels" [Applied Surface Science Advances, 2020; 1: 100031] https://doi.org/10.1016/j.apsadv.2020.100031.

   Declaration of competing interest: The Authors have no interests to declare.

3. "Y–Er–ZrO_2 thermal barrier coatings by EB-PVD: Thermal conductivity, thermal shock life and failure mechanism" [Applied Surface Science Advances, 2021; 3: 100043] https://doi.org/10.1016/j.apsadv.2020.100043.

   Declaration of competing interest: The Authors have no interests to declare.

4. "Integrated solar cells with non-toxic inorganic nanocrystals and polymer bulk heterojunction" [Applied Surface Science Advances, 2021; 3: 100052] https://doi.org/10.1016/j.apsadv.2020.100052.

   Declaration of competing interest: The Authors have no interests to declare.

5. "Morphological and compositional mapping of supersaturated AuNi alloy nanoparticles fabricated by solid state dewetting" [Applied Surface Science Advances, 2021; 4: 100082] https://doi.org/10.1016/j.apsadv.2021.100082.

   Declaration of competing interest: The Authors have no interests to declare.

DOIs of original articles: 10.1016/j.apsadv.2020.100024, 10.1016/j.apsadv.2020.100043, 10.1016/j.apsadv.2021.100082, 10.1016/j.apsadv.2020.100031, 10.1016/j.apsadv.2020.100052

https://doi.org/10.1016/j.apsadv.2021.100108

2666-5239